

MT-HCCAR: Multi-Task Deep Learning with Hierarchical Classification and Attention-based Regression for Cloud Property Retrieval

Xingyan Li*, Andrew M. Sayer^{†‡}, Ian T. Carroll^{†‡}, Xin Huang[§], and Jianwu Wang*

* Department of Information Systems, University of Maryland, Baltimore County, Baltimore, MD, USA

[†]NASA Goddard Space Flight Center, Greenbelt, MD, USA

[‡]Goddard Earth Sciences Technology and Research (GESTAR) II, UMBC, Baltimore, MD, USA

[§]Dept of Computer & Information Sciences, Towson University, Towson, MD, USA

Abstract—In the realm of Earth science, effective cloud property retrieval, encompassing cloud masking, cloud phase classification, and cloud optical thickness (COT) prediction, remains pivotal. Traditional methodologies necessitate distinct models for each sensor instrument due to their unique spectral characteristics. Recent strides in Earth Science research have embraced machine learning and deep learning techniques to extract features from satellite datasets’ spectral observations. However, prevailing approaches lack novel architectures accounting for hierarchical relationships among retrieval tasks. Moreover, considering the spectral diversity among existing sensors, the development of models with robust generalization capabilities over different sensor datasets is imperative. Surprisingly, there is a dearth of methodologies addressing the selection of an optimal model for diverse datasets. In response, this paper introduces MT-HCCAR, an end-to-end deep learning model employing multi-task learning to simultaneously tackle cloud masking, cloud phase retrieval (classification tasks), and COT prediction (a regression task). The MT-HCCAR integrates a hierarchical classification network (HC) and a classification-assisted attention-based regression network (CAR), enhancing precision and robustness in cloud labeling and COT prediction. Additionally, a comprehensive model selection method rooted in K-fold cross-validation, one standard error rule, and two introduced performance scores is proposed to select the optimal model over three simulated satellite datasets OCI, VIIRS, and ABI. The experiments comparing MT-HCCAR with baseline methods, the ablation studies, and the model selection affirm the superiority and the generalization capabilities of MT-HCCAR.

Index Terms—cloud property retrieval, remote sensing, deep learning, multi-task learning

I. INTRODUCTION

The retrieval of cloud properties, denoting the estimation of diverse characteristics of clouds through the analysis of data acquired from remote sensing instruments, plays an essential role in atmospheric and environmental studies. This significance arises from the inherent role of clouds as integral components of the Earth’s atmospheric system, wielding substantial influence over the planet’s energy dynamics, climate regulation, and hydrological cycle [1]. The modulation of surface temperatures and the facilitation of precipitation by clouds underscore their paramount importance in sustaining ecosystems and shaping broader environmental processes.

Satellites serve as invaluable tools for global monitoring of cloud properties, offering an extensive data record of Earth’s

imagery collected by various instruments since the latter part of the previous century. A prominent category of these instruments, commonly referred to as “imagers”, passively collect measurements of the Earth’s surface across multiple wavelength ranges, encompassing the ultraviolet (UV), visible (VIS), near-infrared (NIR), shortwave infrared (SWIR), and thermal infrared (TIR). The data obtained, primarily consisting of observations of reflected solar and/or emitted thermal radiation, undergo routine processing by algorithms. This processing transforms these measurements into geophysical quantities of interest, about both atmospheric and surface characteristics, in a process commonly termed “retrieval”. Routine retrieval of geophysical quantities is key to enhancing the comprehension of Earth’s climate [2]. At the end of such cloud retrieval process, each observed pixel is equipped with estimated values for many cloud properties including cloud mask (whether a pixel is clear or cloudy), cloud thermodynamic phase (liquid droplets or ice crystals), and cloud optical thickness (COT).

One practical motivation for our work is NASA’s Plankton, Aerosol, Cloud, ocean Ecosystem (PACE) mission [3], which will launch in 2024 and advance science in its eponymous disciplines. Heritage cloud masking algorithms are not directly applicable to PACE’s main sensor, the Ocean Color Instrument (OCI) [4], due to different spectral bands compared to algorithms developed for existing sensors. OCI has similarities with some previous spaceborne imagers used for retrieval of cloud (and other) properties such as Moderate Resolution Imaging Spectroradiometer (MODIS) [5], Visible Infrared Imaging Radiometer Suite (VIIRS) [6], and Advanced Baseline Imager (ABI) [7] sensor types. However, two key differences are that 1) OCI has continuous hyperspectral coverage in the UV-NIR, plus discrete SWIR bands, while the others are only multi-spectral (up to a dozen or so discrete relevant bands); and 2) OCI lacks TIR bands. Some of the most commonly used cloud masking tests for those sensors are therefore not applicable, and adapting a subset of those tests would miss out on OCI’s unique abilities, so a new approach is warranted.

Numerous investigations have delved into the application of machine learning techniques for the extraction of cloud proper-

ties from satellite sensor observations. These inquiries encompass both singular cloud property retrievals [8]–[11], as well as the concurrent retrieval of multiple cloud properties [12]–[15]. Nevertheless, challenges and unresolved inquiries persist within the current landscape of machine learning-based cloud retrieval. First, the role of atmospheric domain knowledge, specifically the utilization of physical relationships between cloud mask and cloud phase, in conjunction with advanced machine learning techniques, remains unclear in enhancing the accuracy of cloud retrieval. Second, despite the deployment or design of numerous satellite sensors catering to analogous cloud retrieval tasks (expounded upon in Section III), the feasibility of employing a unified machine learning architecture to facilitate retrieval across different sensors and the generalization ability of such a machine learning model remain uncertain. Third, while there are various metrics to measure machine learning model performance, it remains ambiguous how an overarching ranking system can be established to select an optimal model, especially about determining whether the heightened complexity inherent in newly proposed models is justified in terms of their capabilities.

To address the above challenges, we propose an end-to-end Multi-Task learning architecture with Hierarchical Classification and Attention-assisted Regression (MT-HCCAR) for cloud masking, cloud thermodynamic phase (liquid or ice) prediction, and COT regression. The model consists of a Hierarchical Classification network for cloud masking and cloud phase prediction, and a Classification-assisted Attention-based Regression network (MT-HCCAR) for COT prediction. The classification task is a hierarchical classification (HC) sub-network to capture the hierarchical relationship between ice-crystal cloud and liquid cloud. The COT prediction task is a sub-network integrated with coarse cloud thickness classification (C) using attention mechanism (A) to further enhance regression (R) task accuracy. Our implementation is open-sourced at [16]. Our work’s major contributions are as follows.

- We propose an end-to-end multi-task learning model MT-HCCAR for cloud masking, cloud phase classification, and COT regression. The model utilizes a hierarchical classification approach for cloud masking and cloud phase prediction. Meanwhile, to enhance COT regression accuracy, we use a cross-attention mechanism to learn similarities across the classification task and the regression task. Our extensive experiment results show performance improvement in all tasks using our approach than baseline models.
- We conduct experiments on three satellite sensors (OCI, VIIRS, and ABI, introduced later) to compare different model performances across different satellite products. The results show the generalizability of our proposed model and we analyze our findings from different sensors’ performance.
- To help identify the best model for practical usage, we design a novel model selection method that ranks the performance of different models across multiple metrics

and multiple datasets.

The subsequent sections of this paper are structured as follows: Section II presents an overview of related work in the domains of cloud property retrieval and Multi-Task Learning (MTL) methods for remote sensing. Section III provides an in-depth exploration of the application background, the methodology employed for data simulation, and a precise articulation of our defined problem. Our proposed method, MT-HCCAR, is introduced in Section IV. The assessment metrics and outcomes of our experiments are elucidated in Section V. Section VI outlines our strategies for optimal model selection and presents the corresponding results. Lastly, Section VII encapsulates the paper with concluding remarks.

II. RELATED WORK

Our study focuses on the application of multi-task learning on pixel-wise spectral features from satellite images. This section discusses the existing research on machine learning based cloud property retrieval methods and related work of multi-task learning applied to remote sensing data.

A. Machine learning based cloud property retrieval

In the field of remote sensing, cloud properties encompass a diverse set of characteristics and parameters associated with clouds, which can be observed and measured from a distance using satellite or other remote sensing technologies. These properties include, among others, cloud mask, cloud (thermodynamic) phase, cloud vertical distribution, and COT. Machine learning approaches have demonstrated their efficacy in processing high-dimensional remote sensing data, automatically learning intrinsic features from spectrum data.

In recent years, various machine learning techniques, such as Random Forest (RF), Multi-Layer Perceptron (MLP), and Convolutional Neural Network (CNN), have been employed for retrieving different cloud properties. For instance, Liu et al. [8] utilized Artificial Neural Networks (ANN) and RF for cloud detection using spectral observations and reference labels from the Cloud-Aerosol Lidar with Orthogonal Polarization (CALIOP). Wang et al. [9] proposed an RF-based algorithm using passive spectral observations for cloud detection and phase classification across multiple instruments, evaluating their models against CALIOP and existing VIIRS cloud products. Giuffrida et al. [10] introduced CloudScout, a custom CNN deployed on the Hyperscout-2 nanosatellite payload for onboard cloud detection on hyperspectral images. He et al. [11] proposed a lightweight network, DABNet, for high-accuracy cloud detection based on CNN. Mohajerani et al. [17] presented Cloud-Net, a deep learning-based model using convolutional layers for cloud detection in Landsat 8 imagery. Shao et al. [18] proposed a multi-scale features CNN method for simultaneous classification of imagery into thick, thin, and non-cloud regions, outperforming other cloud detection methods. Jeppesen et al. [19] introduced RS-Net, a deep learning-based cloud detection algorithm for optical satellite imagery, achieving high performance even with a single spectral band. Segal-Rozenhaimer et al. [20] proposed

a domain adversarial neural network (DANN) to enhance the transferability of cloud masks. Huang et al. [14] presented DAMA-WL, an end-to-end deep domain adaptation approach for cloud phase detection, incorporating domain alignment of heterogeneous active and passive satellite remote sensing data. Guo et al. [21] introduced CDnetV2, a CNN-based cloud detection method for remote sensing imagery with cloud-snow coexistence, utilizing attention-based modules for adaptive feature fusion. López-Puigdollers et al. [22] conducted a benchmark of deep learning models for cloud detection in multispectral images, including both rule-based approaches and machine learning approaches.

While these machine learning approaches for cloud property retrieval predominantly leverage spectral features, the main limitations lie in two aspects: 1) many studies do not consider background knowledge, such as the task order (e.g., cloud mask prediction, cloud phase prediction, and COT prediction), and 2) several studies conduct different tasks independently, lacking parameter sharing between classification and regression tasks. These limitations underscore the need for more integrated and informed methodologies in cloud property retrieval studies.

B. Multi-task learning for remote sensing data

Multi-task (MT) learning has emerged as a valuable approach in Earth science and remote sensing applications, facilitating the retrieval of related products from shared features. Recent studies have demonstrated the efficacy of the multi-task learning paradigm in jointly enhancing the performance of diverse tasks.

Ilteralp et al. [23] proposed an MT Convolutional Neural Network (CNN) architecture capable of leveraging unlabeled satellite imagery to predict Chl-a values, incorporating an auxiliary classification task. The proposed MT learning model was compared against alternative approaches, including its single-task regression version, support vector regression, Multi-Layer Perceptron (MLP), morphology-based spectral-spatial approach (EFAL), CNN, and statistical spectral band characteristics known as the band ratio. Zhang et al. [24] introduced MTDR-Net, an MT-driven and reconfigurable network designed to improve cloud detection in regions with coexisting cloud and snow cover in very high-resolution remote sensing images. This model employs an MT gradient flow guidance module (MTGFG) to establish a feature-sharing strategy across different tasks. Chen et al. [25] proposed an MT learning method based on Long Short-Term Memory (LSTM) with an attention mechanism to classify imbalances in wind turbine blades caused by ice accretion. Sarafian et al. [26] presented a meteorology-based model for dust event forecasting, utilizing an MT framework for predicting regional PM10 fields and local *in situ* measured PM10 values. Kim et al. [27] proposed MT CNN and ConvLSTM models for simultaneous forecasting of pixel-wise sea ice concentration, considering both spatial sea ice concentration (SIC) images and temporal sea ice extent (SIE) values. Qiu et al. [28] developed an end-to-end CNN with a shared backbone network

for shared feature learning, attention modules for task-specific feature learning for human settlement extent (HSE) regression, and local climate zone (LCZ) classification. Hanna et al. [29] proposed a U-Net-based architecture to simultaneously predict the pixel area covered by plumes, the type of fired fuel, and the power generation rate from a single-satellite image of a power plant. Ahn et al. [30] presented a systematic approach to forecasting regional wave heights based on different LSTM structures. Zhao et al. [31] introduced a CNN-based framework that combines self-supervised learning and scene classification to improve feature extraction and generalization abilities.

There are also studies conducting ML learning specifically for cloud property retrieval. Yang et al. [12] developed an MLP-based method to retrieve cloud macrophysical parameters (cloud mask, cloud top temperature, and cloud top height) using Himawari-8 satellite data. Wang et al. [13] proposed TIR-CNN based on the U-Net model to retrieve cloud properties including cloud mask, COT, effective particle radius (CER), and cloud top height (CTH) from thermal infrared radiometry. The architecture consists of encoding and decoding layers, convolutional blocks, batch normalization layers, and leaky rectified linear units. The results of applying the model to thermal infrared spectral data from MODIS are used to compare model performance for daytime and nighttime data.

While these above studies offer valuable insights that are beneficial to our design, our work cannot be compared with most of them directly via experiments. It is because of the distinctive nature of our model's output, which manifests at the pixel level rather than the image level. Consequently, architectures employing convolutional layers, such as U-net architecture, are ill-suited for our study's requirements.

III. PROBLEM STATEMENT AND DATA SIMULATION

In this section, we first present the contextual background of the application which includes a forward simulation process and an inverse retrieval process. Then, we delve into a comprehensive exposition of the employed data simulation method in Section III-A, and define our cloud property retrieval problem based on the generated simulation data in Section III-B.

The forward simulation and inverse retrieval processes are characterized as two opposite operations within the context of cloud property analysis. In the forward simulation, spectral bands and physical variables are generated as outputs using cloud properties as input parameters. Conversely, cloud property retrieval involves utilizing spectral features obtained from satellite observations as input, with the resultant output comprising cloud properties such as cloud mask, cloud phase, and COT values. To provide a more explicit formulation, the forward simulation is represented as the mathematical process:

$$\mathbf{X} = f(\mathbf{L}_{cm}, \mathbf{L}_{cph}, \mathbf{Y}_{COT}, \dots) \quad (1)$$

, where $\mathbf{X} = [\mathbf{x}_1, \mathbf{x}_2, \dots, \mathbf{x}_M]$ denotes the spectral and physical features, $f(\cdot)$ represents the simulation algorithm, and $\mathbf{L}_{cm}, \mathbf{L}_{cph}, \mathbf{Y}_{COT}$ are the labels corresponding to cloud mask, cloud phase, and COT values, respectively. Additional

properties are also used as inputs (see Section III-A), but they are not the focus of this work.

Conversely, the inverse retrieval process can be expressed as:

$$\hat{\mathbf{L}}_{cm}, \hat{\mathbf{L}}_{cph}, \hat{\mathbf{Y}}_{COT} = g(\mathbf{X})$$

, where $[\hat{\mathbf{L}}_{cm}, \hat{\mathbf{L}}_{cph}, \hat{\mathbf{Y}}_{COT}]$ represents the predicted values of cloud mask, cloud phase, and COT, as determined by the retrieval algorithm $g(\cdot)$ given the input spectral and physical features \mathbf{X} . Figure 1 illustrates how these two processes operate in our study and the colors of the three sensors show their wavelength band differences.

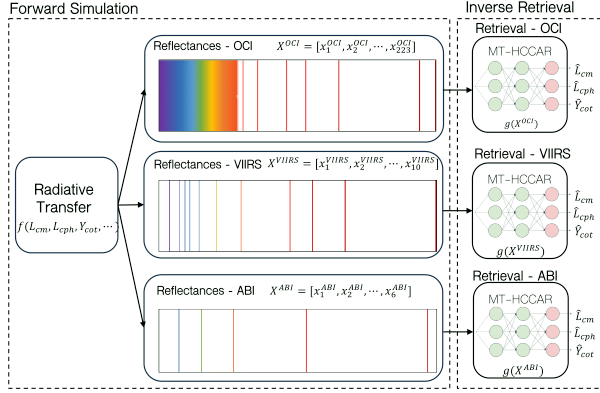


Fig. 1. Illustration of forward simulation and inverse retrieval. Forward simulation uses cloud properties as input parameters to generate spectral bands and physical variables as outputs. Conversely, inverse retrieval entails using spectral features obtained from satellite observations as inputs to generate cloud properties such as cloud mask, cloud phase, and COT values.

A. Forward radiative transfer simulation

Given that OCI has not been launched, simulated datasets for OCI, VIIRS, and ABI are employed for assessing sensors and architectures against a standardized source. Radiative transfer (RT) models play a crucial role by capturing optical processes like scattering and absorption. These models map geophysical parameters, representing surface and atmospheric properties, to spectral intensities at specific detection points—essentially serving as the intermediary link between geophysical quantities and observations made by space-borne sensors.

We cover from ultraviolet (UV) to shortwave infrared (SWIR) and then convolve these hyperspectral simulations with the solar spectrum from [32] and sensor relative spectral response functions for OCI (nominal pre-launch) [4], ABI [7], and VIIRS [6] in order to generate the spectral top of atmosphere reflectance signal that the instruments would observe. This provides our simulated observations and reference truth (i.e., cloud classification and COT), with band centers simulated for each sensor as below:

- **OCI**: 233 bands in total; 226 from the hyperspectral detectors from 350–890 nm (with 2.5 nm spacing between bands) plus seven discrete NIR/SWIR bands centered near 940, 1040, 1250, 1378, 1620, 2130, and 2260 nm.

- **VIIRS**: 10 bands in total, centered near 412, 445, 488, 555, 672, 865, 1240, 1380, 1610, and 2250 nm.
- **ABI**: 6 bands in total, centered near 471, 640, 860, 1370, 1600, and 2200 nm.

Each ABI band has a close analog in VIIRS, and likewise, each VIIRS band has a close analog in OCI, so the trio represent a set of increasing complexity. Both ABI and VIIRS also have thermal infrared (TIR) bands, but these are excluded as the primary motivation for this work is the development of a new methodology for OCI (which does not), and the application to ABI and VIIRS demonstrates the broader applicability of our new architectures.

Inputs for the RT simulation include cloud (phase, microphysical and optical properties, and vertical structure), atmospheric profile (aerosol, gas, Rayleigh scattering, temperature, and pressure), surface (spectral reflectance), and observation (solar and view angles) properties. An ensemble of 250,000 simulations, parameterized by independent samples from realistic distributions of these geophysical properties, form the labeled dataset for model training and evaluation. Distributions and further specifics of the simulations are described in Sayer et al. [33], with two deviations: 1) that study consisted of purely cloud-covered parameterizations; here, 1/3 of simulations corresponded to cloud-free conditions, and the rest to single-layer clouds, and 2) that study considered a narrow spectral range so assumed a spectrally-flat surface albedo; here, we use 20-class extended International Geosphere-Biosphere Program (IGBP) albedo system [34]. These 20 classes correspond to 16 types of land surface spectra (1 desert, 15 non-desert), 1 water surface, and 3 snow/sea ice surfaces. We sampled such that a given simulation had a 1/34 chance of being drawn from each of the 16 “land” spectra, a 9/34 chance of using the “water” spectrum, and a 3/34 of being drawn from each of the “snow/ice” spectra, and for network training classes collapse the 20 spectra into these four main categories (water; snow/ice; desert; non-desert land). The simulation does not include multi-layer or mixed-phase cloud systems, as most satellite retrieval processing algorithms assume a single-layer single-phase cloud system. However, future work could extend the network to be trained (or just evaluated) on an ensemble including such systems.

We emphasize that the software simulates individual point observations (i.e., a pixel) which means that (as is standard for most cloud retrievals in Earth science) the network operates on single pixels at once as opposed to larger scenes (i.e., no spatial context). It would be computationally prohibitive to simulate a globally representative ensemble of satellite scenes, particularly the inclusion of 3D radiative transfer effects. As a result, existing works involving 3D effects [35], [36] have typically been limited to a few case studies.

B. Problem definition for inverse cloud property retrieval

Our primary objective is to accurately model the base-10 logarithm of COT (throughout the remaining text, COT means this logarithm unless explicitly described as the “original” COT) for pixels labeled as cloudy. We work in log space for

COT as this has a more linear relationship with the brightness seen by satellite than the original COT. Simultaneously, the model should be able to accurately classify the cloud phase [cloudy, cloud-free, cloudy-liquid, cloudy-ice] for each pixel in the dataset to aid COT prediction. Therefore, our problem consists of two tasks: 1) a classification task to predict cloud mask and phase, and 2) a regression task to predict COT values. Assuming that the labels are \bar{C} = ‘cloud-free’, C = ‘cloudy’, CL = ‘cloudy-liquid’, and CI = ‘cloudy-ice’, the details of our study are outlined below.

- **Model input.** Our model takes 2-dimensional (2D) data as input that contains a set of sample pixels $S = s_1, s_2, \dots, s_N$, where N is the number of labeled pixels. Each pixel has the following features and target variables.
 - Explanatory features: The input features are represented as $\mathbf{X} = [\mathbf{x}_1, \mathbf{x}_2, \dots, \mathbf{x}_M]$, where M is the dimension of the available features. The exact input feature variables include: 1) surface pressure in millibar (mbar), 2) total column water vapor content in millimeters (mm), 3) total column ozone content in the Dobson unit (DU), 4) types of Earth surface with 4 categories (land, snow, desert, and ocean or water), 5) top of atmosphere reflectance at different wavelengths collected by each spaceborne sensor, 6) viewing zenith angle, solar zenith angle, and the relative azimuth angle, in degree.
 - Cloud mask/phase label (denoted as \mathbf{I}^{cls}): Cloud mask/phase labels are used to train the classification task of the model. The set of possible label values is $l = \{C, \bar{C}, CL, CI\}$.
 - True COT value (denoted as \mathbf{y}^{cot}): the values are used to train the regression task of the model.
- **Model output**
 - Predicted cloud mask/phase class $\hat{\mathbf{I}}^{cls}$ with probabilities \mathbf{u} of each pixel belonging to each of the four classes.
 - Predicted COT value $\hat{\mathbf{y}}^{cot}$ for each pixel.
 - Model parameters β .

Specifically, there are three pieces of background knowledge related to the targeted variables \mathbf{y}^{cot} and \mathbf{I}^{cls} in the dataset for model training.

KNOWLEDGE 1: Original COT values are not available for pixels with no cloud cover, so not every pixel has COT value. That is, if $l_i^{cls} = 0$, then $y_i^{cot} = N/A$.

KNOWLEDGE 2: There is a hierarchical relationship between the labels, as pixels covered by liquid cloud or ice cloud are both cloudy pixels. Thus, CL and CI can be two subclasses of label C = ‘cloudy’.

KNOWLEDGE 3: Each pixel is either a cloudy pixel or a cloud-free pixel, and the cloudy pixel is either classified as a cloudy-liquid pixel or a cloudy-ice pixel. There is no coexistence between liquid cloud and ice cloud in our data. That is, each pixel only be labeled as \bar{C} , or as C together with one of $\{CL, CI\}$.

With the input features \mathbf{X} and true values of the target variables $[\mathbf{y}^{cot}, \mathbf{I}^{cls}]$, we aim to learn a model $\mathcal{M}(\beta)$ such that $[\hat{\mathbf{y}}^{cot}, \hat{\mathbf{I}}^{cls}] = \mathcal{M}(\mathbf{X}|\beta)$.

IV. MT-HCCAR MODEL

Our research objective involves the training of deep learning models to accomplish two tasks: 1) the classification of cloud mask and phase for each pixel based on its reflectance values, and 2) the subsequent prediction of Cloud Optical Thickness (COT) values for pixels classified as cloudy. To address these objectives, we propose an end-to-end Multi-Task Learning (MTL) model, denoted as MT-HCCAR, which integrates a Hierarchical Classification network (HC) and a Classification-assisted with Attention-based Regression network (CAR). Illustrated in Figure 2, the model commences with an encoder, and three branches including Decoder, HC, and CAR follow. Subsequent sections will expound on the individual modules within MT-HCCAR.

A. Encoder-decoder sub-network

An encoder-decoder sub-network, containing an encoder module and a decoder module, is employed in our model to learn latent feature parameters that can be shared for other learning tasks. To integrate the COT regression task and cloud mask/phase prediction task, we adopt the soft-parameter sharing approach of MTL where the shared parameters are derived by encoder-decoder. Previous studies [37], [38] have used similar encoder-decoder techniques to transform original features into more relevant features for better downstream prediction accuracy. In our model, the decoder reconstructs the input feature \mathbf{X} into $\hat{\mathbf{X}}$, and a loss is between \mathbf{X} and $\hat{\mathbf{X}}$ is minimized during training to minimize the distortion of input feature throughout feature extraction layers.

The shared encoder is formed by the first three dense layers, each of which is followed by a ReLU activation function. This feature extractor is a wide-to-narrow structure where the number of kernels at each layer decreases gradually. The decoder and reconstruction branch form a regularized autoencoder which encourages the model to learn features in the aid of the classification task and regression task.

B. Hierarchical classification (HC) sub-network

Utilizing the shared parameters acquired by the encoder-decoder sub-network, MT-HCCAR incorporates a hierarchical classification sub-network. This sub-network comprises a cloud mask classification module and a cloud phase classification module, facilitating cloud mask and phase predictions. To enhance the physical interpretability of the model, the architecture is crafted to mirror human cognitive processes in understanding cloud labels. Fundamentally, to predict cloud phase and Cloud Optical Thickness (COT) values from an Earth science perspective, the model must discern between cloudy and non-cloudy pixels before further classifying liquid-phase and ice-phase pixels and predicting COT values for cloudy pixels.

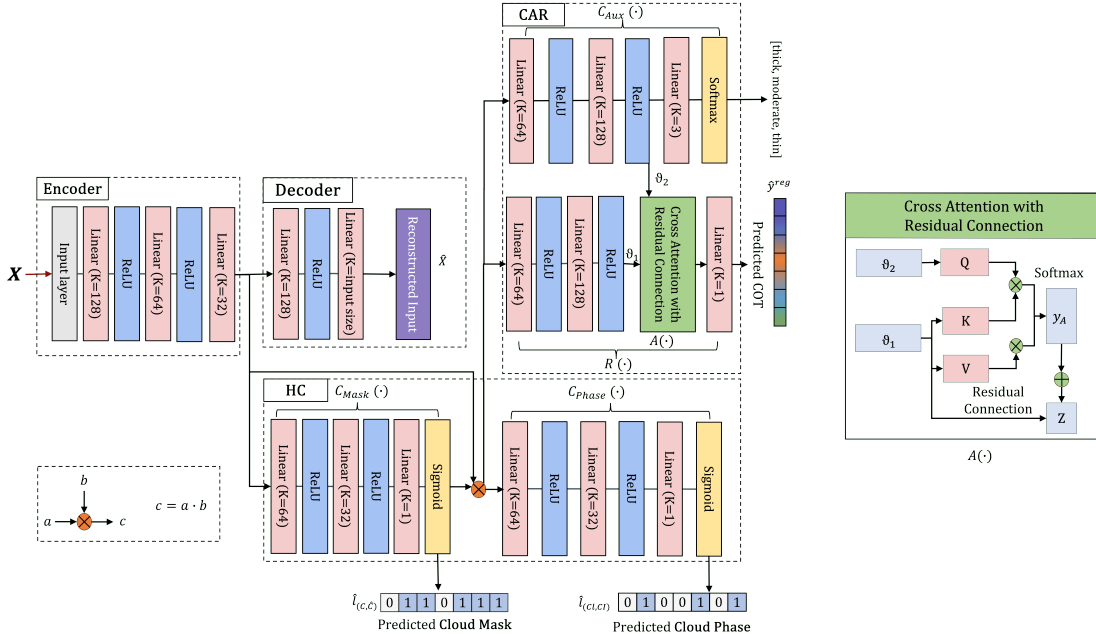


Fig. 2. MT-HCCAR: an end-to-end multi-task learning model with hierarchical classification (HC) and cross attention assisted regression (CAR). The HC sub-network consists of the cloud masking module $C_{Mask}(\cdot)$ and the cloud phase classification module $C_{Phase}(\cdot)$. The CAR sub-network consists of the auxiliary coarse classification module $C_{Aux}(\cdot)$, the cross attention module $A(\cdot)$, and the regression module $R(\cdot)$. On the right is the structure of $A(\cdot)$.

Hierarchical classification has the capability to categorize instances according to label levels, forming a tree-like structure where each label functions as a node on the tree [39]. The HC network used in MT-HCCAR consists of two classifiers $C_{Mask}(\cdot)$ and $C_{Phase}(\cdot)$, the first of which distinguishes cloudy pixels from the cloud-free pixels, and the output is uncertainties for the two labels $[\hat{u}^C, \hat{u}^{\bar{C}}]$. The output uncertainties are binarized to $[\hat{1}^C, \hat{1}^{\bar{C}}]$ by a threshold of 0.5. Before the beginning of the second classifier $C_{Phase}(\cdot)$ input feature \mathbf{X} is multiplied by the predicted cloud label, \hat{y}^C , to filter out cloud-free pixels. Then $C_{Phase}(\cdot)$ classifies liquid-cloud and ice-cloud and the sigmoid uncertainties $[\hat{u}^{CL}, \hat{u}^{CI}]$ are transformed in the same way to binary cloud-phase labels $[\hat{1}^{CL}, \hat{1}^{CI}]$.

C. Classification assisted regression sub-network based on cross attention mechanism (CAR)

Taking inputs from the encoded feature set and cloud mask classification results as input, our regression sub-network is used for further downstream regression prediction of a cloudy pixel’s COT value. Two novel efforts were taken to improve COT prediction accuracy. First, instead of a direct regression module, an auxiliary coarse classification module is added to predict which sub-range of COT each pixel falls into. Second, a residual-based cross-attention mechanism inspired by [40] is developed to enable the regression module and the auxiliary classification module to share relevant correlations and insights.

As illustrated in Figure 2, there is a connection between internal features from the auxiliary classifier and those from the regression network, facilitated by a residual-based cross-

attention module. The close alignment in tasks between the auxiliary classifier and the regression network enables the cross-attention mechanism to selectively attend to features relevant to one task while simultaneously executing the other. This contrasts with relationships involving the regression task and other tasks, such as cloud phase classification, where associations are forged through joint optimization of their respective losses during training iterations, rather than through the shared utilization of internal features.

Our auxiliary coarse classification involves discretizing continuous values into coarse groups, serving as a preprocessing step before regression to align pixels with similar characteristics in the feature space. In MT-HCCAR, an auxiliary classifier is employed to categorize continuous COT values into three distinct levels: thin cloud, moderate cloud, and thick cloud. Specifically, we define thin cloud pixels as those with logarithmic COT values within the range of $[-1.5, 0]$, moderate cloud in $[0, 1]$, and thick cloud in $[1, 2.5]$. Given the analogous nature of the tasks in COT coarse classification and COT regression, the features extracted by the auxiliary classifier are integrated with those obtained from the regression network.

To learn the joint features more effectively, we utilize cross-attention layers to enhance the integration of features from both regression layers and coarse classification layers, facilitating deeper feature learning and more cohesive feature amalgamation. Based on the cross-attention mechanism, adding a residual connection guarantees that the module has stable output and related research such as Wang et al. [41] propose a non-local operation network using a residual connection to insert blocks to the network. By using the residual connection

in our module $A(\cdot)$, the output is

$$A(\vartheta_1, \vartheta_2) = W_z y_A(\vartheta_1, \vartheta_2) + \vartheta_1 \quad (2)$$

, where as shown in Figure 2 ϑ_1 is the feature from the regression network, ϑ_2 is the feature from the auxiliary classification module, W_z is the weight matrix to map y_A to ϑ_2 , and y_A denotes the computation within cross-attention mechanism. The calculation of y_A involves three variables: a query (Q), a key (K) and a value (V) [40]. They are calculated based on corresponding weights matrices W_Q , W_K , W_V learned through model training. $Q = W_Q \vartheta_2$, $K = W_K \vartheta_1$, and $V = W_V \vartheta_1$. Then the y_A in Equation 2 is:

$$y_A = \text{Softmax}(QK^T)V \quad (3)$$

D. Model training of MT-HCCAR

The loss function $\mathcal{L}_{MT-HCCAR}$ for training MT-HCCAR model is formulated as the weighted sum of four components: a hierarchical classification loss \mathcal{L}_{HC} , a regression loss \mathcal{L}_{CAR} , a reconstruction loss \mathcal{L}_{Rec} , and a Lasso regularization loss \mathcal{L}_{Lasso} . That is

$$\mathcal{L} = \mathcal{L}_{HC} + \mathcal{L}_{CAR} + \mathcal{L}_{Rec} + \mathcal{L}_{Lasso} \quad (4)$$

The four loss components are calculated using different rules. The reconstruction loss \mathcal{L}_{Rec} describes the difference between the input features \mathbf{X} and the reconstruction of the input generated through the encoder and the decoder. It is Mean Square Error (MSE) between $\mathbf{D}(\mathbf{X}) = \hat{\mathbf{X}}$ and \mathbf{X} :

$$\mathcal{L}_{Rec} = \sum_{i=1}^n (\mathbf{X}_i - \hat{\mathbf{X}}_i)^2 \quad (5)$$

The Lasso regularization loss component $loss_{l1}$ is an additional penalty to regularize the training process by increasing the sparsity of the model with $l1$ regularization loss:

$$\mathcal{L}_{Lasso} = \lambda \sum_{p=1}^P |\beta_p| \quad (6)$$

The classification loss and regression loss are a weighted sum of losses from the supplement modules. The HC loss is the summation of Binary Cross Entropy loss from cloud masking module $C_{Mask}(\cdot)$ and cloud phase classification module $C_{Phase}(\cdot)$.

$$\mathcal{L}_{HC} = \mathcal{L}_{C_{Mask}} + \mathcal{L}_{C_{Phase}} \quad (7)$$

We have a sigmoid output of cloudy and non-cloud uncertainties $[\hat{u}^C, \hat{u}^{\bar{C}}]$ from cloud mask classifier $C_{Mask}(\cdot)$ and sigmoid output of liquid cloud and ice cloud uncertainties $[\hat{u}^{CL}, \hat{u}^{CI}]$ from cloud phase classifier $C_{Phase}(\cdot)$, then for Equation 7, $\mathcal{L}_{C_{Mask}}$ and $\mathcal{L}_{C_{Phase}}$ are calculated as:

$$\mathcal{L}_{C_{Mask}} = -\frac{1}{N} \sum_{i=1}^N l_i^C \cdot \log(\hat{u}_i^C) + l_i^{\bar{C}} \cdot \log(\hat{u}_i^{\bar{C}}) \quad (8)$$

$$\mathcal{L}_{C_{Phase}} = -\frac{1}{N} \sum_{i=1}^N \hat{u}_i^C l_i^{CL} \cdot \log(\hat{u}_i^C \hat{u}_i^{CL}) + \hat{u}_i^C l_i^{CI} \cdot \log(\hat{u}_i^C \hat{u}_i^{CI}) \quad (9)$$

The CAR loss \mathcal{L}_{CAR} is the summation of Cross Entropy loss from the auxiliary classifier $C_{Aux}(\cdot)$ and $l1$ loss from regression.

$$\mathcal{L}_{CAR} = \mathcal{L}_R + \mathcal{L}_{C_{Aux}}$$

We have predicted COT values and \hat{y}^{cot} and sigmoid output of thickness group uncertainties $[\hat{u}^{thin}, \hat{u}^{mod}, \hat{u}^{thick}]$ from auxiliary classifier, then the regression loss can be formulated as:

$$\mathcal{L}_R = \sum_{i=1}^N |y_i^{cot} - \hat{y}_i^{cot}| \quad (10)$$

$$\mathcal{L}_{C_{Aux}} = -\sum_{i=1}^N \sum_{c \in [thin, mod, thick]} l_i^c \ln \hat{u}_i^c \quad (11)$$

V. EXPERIMENTS

This section presents the comparison with baseline methods and ablation studies, where models are trained by the OCI simulated dataset. Section V-A presents the experimental setup for evaluations. Subsequently, Section V-B introduces the evaluation metrics. Following this, Section V-C and Section V-D undertake a comparative analysis between our model and two baseline methods, evaluating performance in both classification and regression tasks. Ablation experiments are then conducted to discern the significance of the modules employed in our model from an earth science perspective.

A. Experiment setting

The dataset comprises satellite data simulation of instruments OCI, VIIRS and ABI. The three datasets encompassing $N = 250,000$ instances. We split data into 62.5%, 22.5%, and 10.0% for training, validation, and test sets, respectively.

To evaluate our model's performance, we compare MT-HCCAR with six other models on the same dataset OCI. The first two are baseline methods derived from prior studies. The baseline methods are selected from related work with similar task objectives and data formats. Because our dataset contains independent pixels, the baseline methods that can be adapted to our experiments are:

- **Chen et al. (2018)**: A Multi-layer Perceptron (MLP) based method proposed by Chen et al. [42] for cloud property retrieval. We use 1 hidden layer with 10 nodes, which are the same as the authors used.
- **Liu et al. (2022)**: A random forest (RF) based method implemented by Liu et al. [8] for cloud detection. We apply one RF to cloud masking and the same RF to cloud phase classification, respectively. The parameters involved are $n_{trees} = 100$ and $m_{depth} = 10$, which are the best parameters for RF found by the authors.

Besides the above two baseline methods, four ablation study models are also used to evaluate the effectiveness of different modules in our model. In these four models, specific modules

are systematically removed from our proposed model, MT-HCCAR, allowing us to assess the impact of these modifications on model performance.

- **SEQ**: A sequential structure model consists of three separate networks. The first one classifies [cloudy, cloud-free], the second one classifies [liquid-cloud, ice-cloud], and the third network makes regressive predictions on COT for cloudy pixels, respectively.
- **MT-CR**: MTL method combines the classification network and regression network in an end-to-end model.
- **MT-HCR**: Multi-task learning model with the HC network classification task and a regression network in the multi-task learning approach.
- **MT-HCCR**: Multi-task learning model with hierarchical classification and classification-assisted regression. Only the cross-attention module is removed from MT-HCCAR.

After comparing different models on the same dataset OCI, we further use 10-fold cross-validation [43], [44] on four MTL-based models MT-CR, MT-HCR, MT-HCCR, and MT-HCCAR to assess the usefulness of modules and compare the difference in model performance between our models and two existing methods for cloud property retrieval. Additionally, each of the four models will be trained by data from three sensors (OCI, VIIRS, and ABI) respectively.

B. Evaluation metrics

We use three types of metrics to evaluate our work: 1) metrics for the classification task, 2) metrics for the regression task, 3) metrics from an Earth science perspective.

1) *Metrics for classification performance*: We use Accuracy and Average precision to evaluate classification performance.

Cloud masking accuracy (ACC_{bi}): Accuracy is the fraction of correct predictions by our model. We have binary accuracies (ACC_{bi}) between the two big categories [cloudy, cloud-free] and accuracy for each class of [cloud-free, liquid-phase, ice-phase].

$$Accuracy_i = (TP_i + TN_i) / (TP_i + TN_i + FP_i + FN_i) \quad (12)$$

, where TP_i , TN_i , FP_i , and FN_i are the number of true positives, true negatives, false positives, and false negatives for class i , respectively.

Area under precision-recall curve ($AU(\overline{PRC})_w$, $AU(\overline{PRC})_c$): Weighted area under the precision-recall curve ($AU(\overline{PRC})_w$) is the weighted mean of precisions at each threshold h for class i , with the weight as substract between recall at threshold h and the recall at threshold $h-1$. The area under the precision-recall curve for each label $AU(\overline{PRC})_c$ is calculated for each binary label in $l = \{C, \bar{C}, CL, CI\}$. For the weighted area under the precision-recall curve, the recall and the precision at threshold h are:

$$R_w^h = \frac{\sum_l TP_c^h}{\sum_l TP_c^h + \sum_l FN_c^h}, P_w^h = \frac{\sum_l TP_c^h}{\sum_l TP_c^h + \sum_l FP_c^h} \quad (13)$$

And for the area under the precision-recall curve of each label c , the recall and the precision at threshold h are:

$$R_c^h = \frac{TP_c^h}{TP_c^h + FN_c^h}, P_c^h = \frac{TP_c^h}{TP_c^h + FP_c^h} \quad (14)$$

With Equation 13 and Equation 14, $AU(\overline{PRC})_w$ and $AU(\overline{PRC})_c$ are:

$$AU(\overline{PRC})_w = \sum_h (R_w^h - R_w^{h-1}) P_w^h \quad (15)$$

$$AU(\overline{PRC})_c = \sum_h (R_c^h - R_c^{h-1}) P_c^h \quad (16)$$

2) *Metrics for regression performance*: We use MSE and R^2 to evaluate regression performance.

Mean squared error (MSE) is the average squared difference between the true and predicted COT values. We calculate MSE across all classes and MSE for each class of [cloud-free, liquid-phase, ice-phase].

$$MSE = \sum_{i=0}^n (y_i^{cot} - \hat{y}_i^{cot})^2 \quad (17)$$

Coefficient of determination (R^2) measures how close the predicted value is to the true value. R^2 across all classes and R^2 for each class.

$$R^2 = 1 - \frac{\sum_{i=0}^n (y_i^{cot} - \hat{y}_i^{cot})^2}{\sum_{i=0}^n (y_i^{cot} - \bar{y}^{cot})^2} \quad (18)$$

, where \bar{y}^{cot} is the mean value of all true COT values $[y_1^{reg}, y_2^{reg}, \dots, y_n^{reg}]$.

3) *Earth science metrics*: Besides the above commonly used data mining metrics, we also evaluate how a machine learning model could be used for actual satellite missions.

Fraction of pixels meeting PACE goals (FMG) is an evaluation metric defined by the PACE Validation Plan [45] based on scientific requirements and expectations. For each pixel, the relative error $Error_i = \frac{|y^{(cot)_i} - \hat{y}^{(cot)_i}|}{y^{(cot)_i}}$. Then fraction meeting goals represents the percentage of pixels whose relative error is less than 0.25 (for liquid clouds) or 0.35 (for ice clouds).

The Validation Plan defines a predictive model with satisfactory performance as one where this goal is met for 65% of cloudy pixels. Note that this mission goal only applies to cases where the true original COT value is 5 or more ($\log_{10} COT > 0.7$).

C. Comparison with baseline models

Tables I and II present a comprehensive evaluation of our proposed model MT-HCCAR against two baseline methods, demonstrating superior performance across both classification and regression metrics. Specifically, in the assessment of classification tasks, ACC_{bi} pertains to cloud masking performance, while $AU(\overline{PRC})_w$ and $AU(\overline{PRC})_c$ are indicative of cloud phase classification performance.

Upon close examination of Table I, the Random Forest (RF) classifier, as implemented by [8], attains superior ACC_{bi} ,

TABLE I
MODEL PERFORMANCE COMPARISON WITH BASELINE MODELS AND ABLATION STUDY - CLASSIFICATION RESULTS. MODELS ARE TRAINED BY OCI.

MODEL	ACC _{bt}	AU(PRC) _w	AU(PRC) _c			
			Cloudy	Cloud-free	Liquid cloud	Ice cloud
Liu et al.,2022 [8]	0.968	0.985	0.955	0.949	0.951	0.965
Chen et al., 2018 [42]	0.942	0.638	0.974	0.882	0.385	0.348
SEQ	0.963	0.750	0.997	0.978	0.618	0.658
MT-CR	0.965	0.955	0.925	0.925	0.954	0.967
MT-HCR	0.975	0.993	0.999	0.989	0.982	0.992
MT-HCCR	0.982	0.995	0.999	0.992	0.985	0.993
MT-HCCAR	0.984	0.996	0.999	0.995	0.990	0.996

TABLE II
MODEL PERFORMANCE COMPARISON WITH BASELINE MODELS AND ABLATION STUDY - REGRESSION RESULTS. MODELS ARE TRAINED BY OCI.

MODEL	MSE	MSE EACH LABEL		R ²	R ² EACH LABEL		FMG	
		Liquid	Ice		Liquid	Ice	Liquid	Ice
Liu et al.,2022 [8]	-	-	-	-	-	-	-	-
Chen et al., 2018 [42]	0.185	0.193	0.178	0.235	0.247	0.212	43.92%	60.64%
SEQ	0.126	0.133	0.118	0.440	0.274	0.548	4.00%	41.11%
MT-CR	0.062	0.075	0.049	0.728	0.661	0.788	44.46%	68.21%
MT-HCR	0.038	0.045	0.030	0.843	0.810	0.874	65.93%	82.28%
MT-HCCR	0.031	0.035	0.028	0.869	0.854	0.884	66.38%	82.43%
MT-HCCAR	0.026	0.032	0.021	0.891	0.869	0.914	67.96%	82.70%

$AU(\overline{PRC})_w$, and $AU(\overline{PRC})_c$ in comparison to the SEQ model and the simplest Multi-Task Learning (MTL)-based model, MT-CR, within the ablation study. However, MTL-based models featuring the HC module including MT-HCR, MT-HCCR, and MT-HCCAR, surpass the performance of the RF classifier in these metrics.

Turning attention to the Cloud Optical Thickness (COT) regression task, the Multi-Layer Perceptron (MLP)-based baseline method introduced by [42] yields results comparable to the SEQ model, but much worse than MTL-based models. This observation underscores the efficiency of MTL-based models for of COT regression.

D. Ablation study

The outcomes obtained from models SEQ through MT-HCCAR in Table I and Table II underscore the efficacy of our MTL structure and the incorporated modules, namely Hierarchical Classification (HC) and Cross-Attention Residual (CAR), in enhancing both classification and regression performances. A comparative analysis reveals notable improvements across all metrics when contrasting the results of models through SEQ to MT-HCCAR. Specifically, when compared to the MT-CR model, the introduction of hierarchical classification MT-HCR demonstrates superior accuracy in binary classification ([cloudy, cloud-free]) and further refines the classification of liquid and ice cloud phases, thereby contributing to enhancements in all regression metrics. The performance of the model does not see any drop from MT-HCR to MT-HCCAR, even though the models focus on improving regression by using CAR.

Moreover, the efficacy of the CAR module is validated in the comparison between MT-HCCAR and MT-HCR, showcasing its utility in improving both classification and regression outcomes. Furthermore, the adoption of the cross-attention

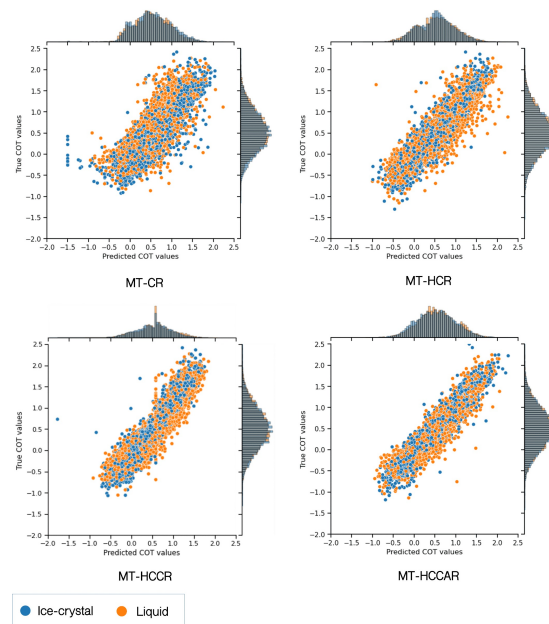


Fig. 3. Scatter plot with PDF distribution of true COT values (y-axis) and predicted COT values (x-axis).

module is substantiated by the superior performance observed in MT-HCCR compared to MT-HCCAR, underscoring the module’s effectiveness in facilitating information exchange between hierarchical classification and regression tasks.

In order to visually depict the enhancements facilitated by the HC module and the CAR module, Figure 3 presents a scatter plot illustrating the distribution of ground truth Cloud Optical Thickness (COT) values and the corresponding predicted COT values for all instances within the test set. The integration of the HC module and CAR module in our model

yields more accurate predictions compared to MT-CR and MT-HCR, as evidenced by two notable observations in the figure. Firstly, the Probability Density Function (PDF) distribution of predictions closely aligns with the true distribution, indicating an improved fidelity to the actual COT values. Secondly, the scatter points exhibit a greater concentration along the diagonal line, further corroborating the model’s enhanced precision when incorporating the HC and CAR modules.

E. Earth science evaluation

1) *Applicability for satellite mission:* Satellite-derived cloud masks are generally evaluated either through comparison against a human-labeled image set, or against ground-based, airborne, or spaceborne observations from sensors that have much greater sensitivity for cloud detection than the image in question (typically active sensors such as radar and/or lidar). Accuracies tend to depend on surface type and illumination conditions; for daytime scenes such as those simulated here, some reported accuracies for NASA’s widely-used MODIS cloud mask are 0.850 (Ackerman et al. [46]), 0.778 (Wang et al. [47]), and 0.894 (Kotarba [48]). Accuracy tends to be worse than average in polar regions and better for non-polar land and ocean [49]. Most commonly it is optically thin clouds (e.g. subvisual cirrus) that are missed. For instance, Ackerman et al. [46] found that 90% of misclassified pixels in MODIS over a vegetated ground site in the USA had a COT under 0.4. Chen et al. [42] developed an NN cloud mask for MODIS, also based on RT simulations, and found an accuracy of 0.985 on training data but lower accuracies in the range of 0.739-0.885 on real data depending on region and time of year. Although real-world conditions are more complex than a simulation, and each sensor’s measurement characteristics result in different sensitivity to clouds, the results suggest our models’ accuracies are competitive with current approaches. Note, that the cloud phase is less commonly validated in this way.

Obtaining a validation-grade COT measurement is exceptionally challenging, and reference datasets for COT lack the comprehensive coverage available for other cloud properties like cloud mask and cloud height [50]. Consequently, existing comparisons primarily focus on assessing agreement levels among different remotely sensed datasets. As previously mentioned, the PACE mission aims to achieve an error rate of less than 25% (for liquid clouds) or 35% (for ice clouds) in determining COT for clouds with true COT > 5, at least 65% of the time. Our network’s performance indicates its potential to meet these objectives. Notably, the larger allowable uncertainty for ice clouds in the PACE mission is rooted in the expectation that accurate determination would be more challenging due to significant variations in ice crystal shape, size, and roughness in real-world scenarios. In contrast, our results demonstrate that the predicted uncertainty for ice COT can be smaller than that for liquid COT. Conventional approaches often assume specific ice crystal shapes and roughness, leading to increased uncertainty in retrieved ice COT. Our findings suggest that satellite measurements inherently contain information related to these parameters, which the networks are adept at learning.

2) *Performance of different satellite sensors:* The classification tasks exhibit high accuracies across all sensors, with virtually indistinguishable performance from a scientific perspective. This uniformity is unsurprising, despite the considerable variance in the number of bands among sensors. The fundamental nature of cloud masking in Earth science prompts many sensors to incorporate a common set of bands proven to be effective for this purpose, with additional bands often designed for diverse applications. For instance, OCI’s hyperspectral bands support the measurement of different ocean plankton species [3], revealing subtle spectral differences not readily discernible in multispectral data. In the regression task, OCI and VIIRS outperform ABI, indicating the utility of additional bands in predicting COT. The unexpectedly slightly superior performance of VIIRS over OCI may suggest that OCI’s substantially larger feature space makes finding an optimal solution during training more challenging or could be attributed to stochastic variation. Adding training epochs for OCI may lead to better results.

VI. STRATEGIES FOR SELECTING THE OPTIMAL MODEL

Based on the evaluation metrics and experiment results expounded in Section V, our analysis extends to the application of the MT models to three different sensors simulated datasets, namely OCI, VIIRS, and ABI. Given the diverse evaluation metrics and the utilization of different satellite datasets, it is imperative to identify the singular optimal model among our multi-task learning-based models, namely MT-CR, MT-HCR, and MT-HCCAR, to be implemented on different datasets.

The process of model selection is based on the four metrics: ACC_{bi} , $AU(\overline{PRC})_w$, MSE, and R^2 . The process includes 3 steps: 1) employing K-fold cross-validation, 2) executing one standard error rule (1SE rule), and 3) computing performance scores. Initially, K-fold cross-validation is employed to compare the model’s absolute performance using the mean value of each metric over K folds. This involves aggregating the mean values of all four metrics across models trained on each dataset over K folds. Subsequently, the one standard error rule is applied to assess the balance between model absolute performance and computational complexity.

While the first and second steps prove effective in selecting the optimal model within the confines of a single metric and a single dataset, extending this evaluation to encompass all datasets and all metrics requires the introduction of absolute performance scores (P_{ab} and 1SE performance scores), denoted as P_{1SE} . These proposed scores serve as comprehensive indicators for selecting a single model that excels across diverse datasets and evaluation metrics. Table III shows collected metrics and performance scores for each model and each dataset. The following paragraphs will describe K-fold cross-validation, one standard error rule, and our proposed performance score, respectively.

We note our model selection method is also useful for other multi-task learning applications due to the multi-objective nature of such applications and our method’s capability of considering multiple metrics and datasets.

TABLE III
MODEL SELECTION USING K-FOLD CROSS-VALIDATION AND 1SE RULE.

DATASET	MODEL	$\mu(Metric)$	$SE(Metric)$	1SE RANGE	$P_{ab}^{\mathcal{M},\mathcal{D}}$	$P_{1SE}^{\mathcal{M},\mathcal{D}}$
MEAN VALUE OF ACC_{bi} OVER 10 FOLDS						
OCI	MT-CR	0.969	7.608E-04	[0.969, 0.970]	-1.54%	0
	MT-HCR	0.984	6.741E-04	[0.983, 0.985]	-0.04%	1
	MT-HCCAR	0.985	1.057E-03	[0.983, 0.986]	0.00%	0
VIIRS	MT-CR	0.976	6.866E-04	[0.975, 0.976]	-1.39%	0
	MT-HCR	0.989	5.027E-04	[0.988, 0.989]	-0.04%	1
	MT-HCCAR	0.989	4.961E-04	[0.989, 0.990]	0.00%	0
ABI	MT-CR	0.973	1.229E-03	[0.972, 0.974]	-1.37%	0
	MT-HCR	0.986	4.716E-04	[0.986, 0.987]	-0.03%	1
	MT-HCCAR	0.987	6.180E-04	[0.986, 0.987]	0.00%	0
MEAN VALUE OF $AU(PRC)_w$ OVER 10 FOLDS						
OCI	MT-CR	0.953	1.60E-03	[0.951, 0.954]	-4.29%	0
	MT-HCR	0.995	2.83E-04	[0.995, 0.995]	-0.04%	0
	MT-HCCAR	0.996	2.08E-04	[0.995, 0.996]	0.00%	1
VIIRS	MT-CR	0.939	3.17E-02	[0.908, 0.971]	-5.78%	0
	MT-HCR	0.996	1.88E-04	[0.996, 0.997]	-0.06%	0
	MT-HCCAR	0.997	1.37E-04	[0.997, 0.997]	0.00%	1
ABI	MT-CR	0.969	2.19E-03	[0.967, 0.971]	-2.75%	0
	MT-HCR	0.996	1.62E-04	[0.996, 0.996]	0.00%	1
	MT-HCCAR	0.996	1.67E-04	[0.996, 0.996]	-0.02%	0
MEAN VALUE OF MSE OVER 10 FOLDS						
OCI	MT-CR	0.055	2.916E-03	[0.058, 0.052]	-100.00%	0
	MT-HCR	0.034	5.970E-04	[0.034, 0.035]	-25.27%	0
	MT-HCCAR	0.027	4.910E-04	[0.028, 0.027]	0.00%	1
VIIRS	MT-CR	0.043	2.075E-03	[0.045, 0.041]	-76.48%	0
	MT-HCR	0.030	8.104E-04	[0.031, 0.029]	-21.65%	0
	MT-HCCAR	0.025	1.282E-03	[0.026, 0.023]	0.00%	1
ABI	MT-CR	0.057	1.519E-03	[0.059, 0.056]	-78.86%	0
	MT-HCR	0.038	5.714E-04	[0.039, 0.038]	-19.48%	0
	MT-HCCAR	0.032	3.121E-04	[0.032 , 0.032]	0.00%	1
MEAN VALUE OF R^2 OVER 10 FOLDS						
OCI	MT-CR	0.758	1.24E-02	[0.770, 0.746]	-14.25%	0
	MT-HCR	0.854	2.55E-03	[0.857, 0.851]	-3.39%	0
	MT-HCCAR	0.884	2.35E-03	[0.882, 0.886]	0.00%	1
VIIRS	MT-CR	0.810	9.62E-03	[0.800, 0.820]	-9.72%	0
	MT-HCR	0.874	3.59E-03	[0.870, 0.878]	-2.58%	0
	MT-HCCAR	0.897	5.30E-03	[0.892, 0.902]	0.00%	1
ABI	MT-CR	0.751	7.44E-03	[0.743, 0.758]	-13.25%	0
	MT-HCR	0.840	2.20E-03	[0.838, 0.843]	-2.91%	0
	MT-HCCAR	0.866	1.51E-03	[0.864, 0.867]	0.00%	1

A. K-fold cross-validation and 1SE rule

K-fold cross-validation is used to compare the absolute performance of each model \mathcal{M} trained by each dataset \mathcal{D} based on mean values of the four evaluation metrics over K folds. We use the number of folds $K = 10$ because this value has been found through experiments to generally result in a model skill estimate with low bias and modest variance [44], [51]. For each fold, $(K - 1)N/K$ pixels are in the training set, and the left N/K pixels are in the test set. **Mean values** $\mu(Metric)$ of four evaluation metrics over 10 folds are calculated for each experiment to compare differences in model absolute performance. Among the four metrics, Acc_{bi} and $AU(PRC)_w$ access the classification task while MSE and R^2 access the regression task. The mean value of a certain metric $Metric$ over 10 folds $\mu(Metric)$ is: $\mu(Metric) = \frac{1}{K} \sum_{k=1}^{K=10} Metric^{k,\mathcal{M}^{\mathcal{D}}}$, where $Metric^k$ is $Metric$ for fold k of model \mathcal{M} trained by dataset \mathcal{D} .

With the mean values from K-fold cross validation, we then use **one standard error rule (1SE rule)** [52] to select

the most parsimonious model for each dataset. The mean of evaluation metrics, computed over 10 folds, provides an absolute measure of model accuracy. However, it is essential to consider the trade-off between model complexity and absolute performance, as this balance is crucial for assessing the overall quality of a model. Therefore, in addition to the mean value, we also calculate the region defined by one standard error rule (1SE region) of each metric. With the 1SE range of each metric, we need to select ‘‘1SE region of the best’’, which is the 1SE range of the model with minimum mean error. Then the simplest model whose mean falls within 1SE region of the best is the most parsimonious model according to 1SE rule [43], [53]. Under our experiment setting, the **standard error** for a certain metric $SE(Metric)$ is calculated as:

$$SE(Metric) = \frac{s}{\sqrt{K}} \quad (19)$$

, where s is the square root of variance s^2 for $Metric$ over 10 folds. Then the 1SE region of each model is defined as: $[\mu - SE, \mu + SE]$.

In our experimental analyses, we derive the following conclusion regarding the application of the 1SE rule: if none of the $\mu(Metric)$ values for alternative models lie within the 1SE region of the optimal model, the model exhibiting the highest mean metric value is the preferred choice based on this specific metric.

B. The absolute score and the 1SE rule score

Despite conducting K-fold cross-validation and 1SE rule, we still need a method to describe the general model performance across all four evaluation metrics and all three datasets. Here we introduced the absolute performance score and the 1SE rule score.

To describe the absolute performance based on the mean value as well as the model selection results based on the 1SE rule for each model over all datasets and all metrics, we propose to use **absolute performance score** P_{ab} and **1SE score** P_{1SE} . The absolute performance score P_{ab} describes how worse other models are than the model with the best absolute performance. The performance score for each model is calculated by the following formula:

$$\begin{aligned} P_{ab}^{\mathcal{M}} &= \sum_D \sum_{Metric} P_{ab}^{\mathcal{M}, \mathcal{D}} \\ &= \sum_D \sum_{Metric} \frac{\mu(Metric)^{\mathcal{M}^{\mathcal{D}}} - \mu(Metric)^{\mathcal{M}_\mu^{\mathcal{D}^*}}}{\mu(Metric)^{\mathcal{M}_\mu^{\mathcal{D}^*}}} \end{aligned} \quad (20)$$

, where components $P_{ab}^{\mathcal{M}, \mathcal{D}}$ is the score for a specific model \mathcal{M} applied to a specific dataset \mathcal{D} , $\mu(Metric)^{\mathcal{M}^{\mathcal{D}}}$ is the mean value of a specific metric $Metric$ of model $\mathcal{M}^{\mathcal{D}}$ applied to dataset \mathcal{D} , and $\mathcal{M}_\mu^{\mathcal{D}^*}$ is the model with the best mean value for dataset \mathcal{D} .

The 1SE performance score is the weighted sum of counts that the model is selected according to the 1SE rule across all metrics and all datasets. The component $P_{1SE}^{\mathcal{M}, \mathcal{D}}$ is the 1SE performance score for model \mathcal{M} applied to dataset \mathcal{D} . The calculation of the total score P_{1SE} for model \mathcal{M} is:

$$\begin{aligned} P_{1SE}^{\mathcal{M}} &= \sum_D \mathbf{w}_m \sum_{Metric} P_{1SE}^{\mathcal{M}, \mathcal{D}} \\ &= \sum_D \sum_{Metric} \psi(\mu(Metric), \mu(\mathcal{M}, \mathcal{D})) \end{aligned} \quad (21)$$

, where $\psi(\cdot)$ is a rule that if Model \mathcal{M} trained by dataset \mathcal{D} is selected by 1SE rule based on the mean value of a certain metric, then $\psi(\cdot)$ outputs 1, and otherwise 0. Weights $\mathbf{w}_m = [w_{Acc_{bi}}, w_{AU(\overline{PRC})_w}, w_{MSE}, w_{R^2}]$ define the significance of four metrics. We set $\mathbf{w}_m = [1, 1, 1, 1]$ in our experiments because we consider the classification task and regression task equally important in our application. We will further discuss the model performance shown in Table III based on 1SE region of the best to show that MT-HCCAR is optimal based on all four metrics of Acc_{bi} , $AU(\overline{PRC})_w$, MSE, and R^2 .

C. Model selection results

This section discusses the superior performance of our proposed MT-HCCAR model, evident in its highest absolute

performance score $P_{ab}^{\mathcal{M}}$ score and the top 1SE rule score $P_{1SE}^{\mathcal{M}}$. The last two columns of Table III are components of $P_{ab}^{\mathcal{M}}$ and $P_{1SE}^{\mathcal{M}}$. Utilizing Equation 20, the absolute performance scores for each model are calculated as follows: $P_{ab}^{MT-CR} = -4.12\%$, $P_{ab}^{MT-HCR} = -0.21\%$, and $P_{ab}^{MT-HCCAR} = -0.02\%$. The highest $P_{ab}^{\mathcal{M}}$ indicates that MT-HCCAR exhibits the best mean value across all evaluation metrics, including Acc_{bi} , $AU(\overline{PRC})_w$, and R^2 , across all satellite datasets.

Furthermore, MT-HCCAR achieves the most substantial $P_{1SE}^{\mathcal{M}}$. By using Equation 21, the 1SE performance scores for each model are calculated as follows: $P_{1SE}^{MT-CR} = 0$, $P_{1SE}^{MT-HCR} = 4$, $P_{1SE}^{MT-HCCAR} = 8$. Achieving the highest $P_{1SE}^{\mathcal{M}}$ suggests that all other models exhibit mean values beyond the 1 standard error (1SE) range of MT-HCCAR. This implies that MT-HCCAR avoids overfitting in comparison to other models, considering model complexity. This finding further establishes MT-HCCAR as the optimal model for implementation across various satellite datasets.

Additionally, MT-HCCAR exhibits higher mean values and a narrower 1SE range compared to alternative models, indicating superior generalization. In summary, MT-HCCAR, adhering to the 1SE rule, demonstrates superior performance in both classification and regression tasks, surpassing other models without succumbing to overfitting.

VII. CONCLUSIONS

In this study, we present MT-HCCAR, an end-to-end multi-task learning model tailored for cloud property retrieval on simulated OCI satellite dataset in the PACE project, tackling tasks including cloud masking, cloud phase classification, and Cloud Optical Thickness (COT) prediction. The model is implemented on three sensors' simulated datasets (OCI, VIIRS, and ABI), respectively, to examine its generalization. Comparative analyses against two baseline methods and ablation studies underscore the effectiveness of the Hierarchical Classification (HC) module and the Classification-Assisted with Attention-based Regression (CAR) module, enhancing performance in both classification and regression tasks. Moreover, our model selection approach, incorporating K-fold cross-validation, the 1SE rule, and two novel performance scores, establishes MT-HCCAR's superior performance across different datasets and multiple evaluation metrics. The positive results affirm our model's capability to address real-world challenges in cloud property retrieval and other multi-task applications. Future research endeavors will involve applying the model to actual OCI data, co-located in space and time with VIIRS and ABI post-PACE launch, to assess its performance, and consistency, and enable detailed comparisons with traditional (non-machine-learning) approaches.

ACKNOWLEDGMENT

This work is supported by a student fellowship from Goddard Earth Sciences Technology and Research (GESTAR) II, UMBC, grant OAC-1942714 from the National Science Foundation (NSF) and grant 80NSSC21M0027 from the National Aeronautics and Space Administration (NASA).

REFERENCES

- [1] Aiko Voigt, Nicole Alber, Paulo Ceppi, Kevin Grise, Ying Li, and Brian Medeiros. Clouds, radiation, and atmospheric circulation in the present-day climate and under climate change. *Wiley Interdisciplinary Reviews: Climate Change*, 12(2):e694, 2021.
- [2] R. Hollmann, C. J. Merchant, R. Saunders, C. Downy, M. Buchwitz, A. Cazenave, E. Chuvieco, P. Defourny, G. de Leeuw, R. Forsberg, T. Holzer-Popp, F. Paul, S. Sandven, S. Sathyendranath, M. van Roozendael, and W. Wagner. The esa climate change initiative: Satellite data records for essential climate variables”. *Bulletin of the American Meteorological Society*, 94(10):1541 – 1552, 2013.
- [3] P. Jeremy Werdell, Michael J. Behrenfeld, Paula S. Bontempi, Emmanuel Boss, Brian Cairns, Gary T. Davis, Bryan A. Franz, Ulrik B. Gliese, Eric T. Gorman, Otto Hasekamp, Kirk D. Knobelspiesse, Antonio Mannino, J. Vanderlei Martins, Charles R. McClain, Gerhard Meister, and Lorraine A. Remer. The plankton, aerosol, cloud, ocean ecosystem mission: Status, science, advances. *Bulletin of the American Meteorological Society*, 100(9):1775 – 1794, 2019.
- [4] Ocean Color Instrument (OCI) Sensor. <https://oceancolor.gsfc.nasa.gov/data/pace/characterization/>.
- [5] Moderate Resolution Imaging Spectroradiometer (MODIS) Sensor. <https://modis.gsfc.nasa.gov/>.
- [6] Visible Infrared Imaging Radiometer Suite (VIIRS) Sensor. <https://ncc.nesdis.noaa.gov/VIIRS/VIIRSSpectralResponseFunctions.php>.
- [7] Advanced Baseline Imager (ABI) Sensor. <https://ncc.nesdis.noaa.gov/GOESR/ABI.php>.
- [8] Chao Liu, Shu Yang, Di Di, Yuanjian Yang, Chen Zhou, Xiuqing Hu, and Byung-Ju Sohn. A machine learning-based cloud detection algorithm for the himawari-8 spectral image. *Advances in Atmospheric Sciences*, 39(12):1994–2007, 2022.
- [9] Chenxi Wang, Steven Platnick, Kerry Meyer, Zhibo Zhang, and Yaping Zhou. A machine-learning-based cloud detection and thermodynamic-phase classification algorithm using passive spectral observations. *Atmospheric Measurement Techniques*, 13(5):2257–2277, 2020.
- [10] Gianluca Giuffrida, Lorenzo Diana, Francesco de Gioia, Gionata Benelli, Gabriele Meoni, Massimiliano Donati, and Luca Fanucci. Cloudscout: A deep neural network for on-board cloud detection on hyperspectral images. *Remote Sensing*, 12(14):2205, 2020.
- [11] Qibin He, Xian Sun, Zhiyuan Yan, and Kun Fu. Dabnet: Deformable contextual and boundary-weighted network for cloud detection in remote sensing images. *IEEE Transactions on Geoscience and Remote Sensing*, 60:1–16, 2021.
- [12] Yikun Yang, Wenxiao Sun, Yulei Chi, Xing Yan, Hao Fan, Xingchuan Yang, Zhanshan Ma, Quan Wang, and Chuanfeng Zhao. Machine learning-based retrieval of day and night cloud macrophysical parameters over east asia using himawari-8 data. *Remote Sensing of Environment*, 273:112971, 2022.
- [13] Quan Wang, Chen Zhou, Xiaoyong Zhuge, Chao Liu, Fuzhong Weng, and Minghuai Wang. Retrieval of cloud properties from thermal infrared radiometry using convolutional neural network. *Remote Sensing of Environment*, 278:113079, 2022.
- [14] Xin Huang, Sahara Ali, Chenxi Wang, Zeyu Ning, Sanjay Purushotham, Jianwu Wang, and Zhibo Zhang. Deep domain adaptation based cloud type detection using active and passive satellite data. In *2020 IEEE International Conference on Big Data (Big Data)*, pages 1330–1337, 2020.
- [15] Xin Huang, Chenxi Wang, Sanjay Purushotham, and Jianwu Wang. Vdam: Vae based domain adaptation for cloud property retrieval from multi-satellite data. In *Proceedings of the 30th International Conference on Advances in Geographic Information Systems*. ACM SIGSPATIAL, 2022.
- [16] GitHub Repository of Multi-Task Deep Learning with Hierarchical Classification and Attention-based Regression for Cloud Property Retrieval (MT-HCCAR). <https://github.com/AI-4-atmosphere-remote-sensing/MT-HCCAR>.
- [17] Sorour Mohajerani and Parvaneh Saeedi. Cloud-net: An end-to-end cloud detection algorithm for landsat 8 imagery. In *IGARSS 2019-2019 IEEE International Geoscience and Remote Sensing Symposium*, pages 1029–1032. IEEE, 2019.
- [18] Zhenfeng Shao, Yin Pan, Chunyuan Diao, and Jiajun Cai. Cloud detection in remote sensing images based on multiscale features-convolutional neural network. *IEEE Transactions on Geoscience and Remote Sensing*, 57(6):4062–4076, 2019.
- [19] Jacob Høxbroe Jeppesen, Rune Hylsberg Jacobsen, Fadil Inceoglu, and Thomas Skjødeberg Toftegaard. A cloud detection algorithm for satellite imagery based on deep learning. *Remote sensing of environment*, 229:247–259, 2019.
- [20] Michal Segal-Rozenhaimer, Alan Li, Kamalika Das, and Ved Chirayath. Cloud detection algorithm for multi-modal satellite imagery using convolutional neural-networks (cnn). *Remote Sensing of Environment*, 237:111446, 2020.
- [21] Jianhua Guo, Jingyu Yang, Huanjing Yue, Hai Tan, Chunping Hou, and Kun Li. Cdnv2: Cnn-based cloud detection for remote sensing imagery with cloud-snow coexistence. *IEEE Transactions on Geoscience and Remote Sensing*, 59(1):700–713, 2020.
- [22] Dan López-Puigdollers, Gonzalo Mateo-García, and Luis Gómez-Chova. Benchmarking deep learning models for cloud detection in landsat-8 and sentinel-2 images. *Remote Sensing*, 13(5):992, 2021.
- [23] Melike Ilteralp, Sema Ariman, and Erchan Aptoula. A deep multitask semisupervised learning approach for chlorophyll-a retrieval from remote sensing images. *Remote Sensing*, 14(1):18, 2021.
- [24] Guangbin Zhang, Xianjun Gao, Jinhui Yang, Yuanwei Yang, Meilin Tan, Jie Xu, and Yanjun Wang. A multi-task driven and reconfigurable network for cloud detection in cloud-snow coexistence regions from very-high-resolution remote sensing images. *International Journal of Applied Earth Observation and Geoinformation*, 114:103070, 2022.
- [25] Jianjun Chen, Weihao Hu, Di Cao, Zhenyuan Zhang, and Zhe Chen. A novel multi-task learning method with attention mechanism for wind turbine blades imbalance fault diagnosis. In *2022 4th Asia Energy and Electrical Engineering Symposium (AEEES)*, pages 857–862. IEEE, 2022.
- [26] Ron Sarafian, Dori Nissenbaum, Shira Raveh-Rubin, Vikhyat Agrawal, and Yinon Rudich. Deep multi-task learning for early warnings of dust events implemented for the middle east. *Npj climate and atmospheric science*, 6(1):23, 2023.
- [27] Eliot Kim, Peter Kruse, Skylar Lama, Jamal Bourne, Michael Hu, Sahara Ali, Yiyi Huang, and Jianwu Wang. Multi-task deep learning based spatiotemporal arctic sea ice forecasting. In *2021 IEEE International Conference on Big Data (Big Data)*, pages 1847–1857. IEEE, 2021.
- [28] Chunping Qiu, Lukas Liebel, Lloyd Haydn Hughes, Michael Schmitt, Marco Körner, and Xiao Xiang Zhu. Multitask learning for human settlement extent regression and local climate zone classification. *IEEE Geoscience and Remote Sensing Letters*, 19:1–5, 2020.
- [29] Joëlle Hanna, Damian Borth, and Michael Mommert. Physics-guided multitask learning for estimating power generation and co₂ emissions from satellite imagery. *IEEE Transactions on Geoscience and Remote Sensing*, 2023.
- [30] Seongho Ahn, Trung Duc Tran, and Jongho Kim. Systematization of short-term forecasts of regional wave heights using a machine learning technique and long-term wave hindcast. *Ocean Engineering*, 264:112593, 2022.
- [31] Zhicheng Zhao, Ze Luo, Jian Li, Can Chen, and Yingchao Piao. When self-supervised learning meets scene classification: Remote sensing scene classification based on a multitask learning framework. *Remote Sensing*, 12(20):3276, 2020.
- [32] Odele M Coddington, Erik C Richard, Dave Harber, P Pilewskie, Thomas N Woods, K Chance, Xiong Liu, and Kang Sun. The tsis-1 hybrid solar reference spectrum. *Geophysical research letters*, 48(12):e2020GL091709, 2021.
- [33] Andrew M Sayer, Luca Lelli, Brian Cairns, Bastiaan van Diedenhoven, Amir Ibrahim, Kirk D Knobelspiesse, Sergey Korkin, and P Jeremy Werdell. The chroma cloud-top pressure retrieval algorithm for the plankton, aerosol, cloud, ocean ecosystem (pace) satellite mission. *Atmospheric Measurement Techniques*, 16(4):969–996, 2023.
- [34] Claudia Emde, Robert Buras-Schnell, Arve Kylling, Bernhard Mayer, Josef Gasteiger, Ulrich Hamann, Jonas Kylling, Bettina Richter, Christian Pause, Timothy Dowling, et al. The libradtran software package for radiative transfer calculations (version 2.0. 1). *Geoscientific Model Development*, 9(5):1647–1672, 2016.
- [35] Zhibo Zhang, Andrew S Ackerman, Graham Feingold, Steven Platnick, Robert Pincus, and Huiwen Xue. Effects of cloud horizontal inhomogeneity and drizzle on remote sensing of cloud droplet effective radius: Case studies based on large-eddy simulations. *Journal of Geophysical Research: Atmospheres*, 117(D19), 2012.
- [36] Steven Massie, Heather Cronk, Aronne Merrelli, Sebastian Schmidt, and Steffen Mauzeri. Insights into 3d cloud radiative transfer for oco-2. *Atmospheric Measurement Techniques Discussions*, 2022:1–40, 2022.

- [37] Shubham Toshniwal, Hao Tang, Liang Lu, and Karen Livescu. Multitask learning with low-level auxiliary tasks for encoder-decoder based speech recognition. *arXiv preprint arXiv:1704.01631*, 2017.
- [38] Ryohei Kuga, Asako Kanezaki, Masaki Samejima, Yusuke Sugano, and Yasuyuki Matsushita. Multi-task learning using multi-modal encoder-decoder networks with shared skip connections. In *Proceedings of the IEEE International Conference on Computer Vision Workshops*, pages 403–411, 2017.
- [39] Fábio M Miranda, Niklas Köhnecke, and Bernhard Y Renard. Hiclass: a python library for local hierarchical classification compatible with scikit-learn. *Journal of Machine Learning Research*, 24(29):1–17, 2023.
- [40] Ashish Vaswani, Noam Shazeer, Niki Parmar, Jakob Uszkoreit, Llion Jones, Aidan N Gomez, Łukasz Kaiser, and Illia Polosukhin. Attention is all you need. *Advances in neural information processing systems*, 30, 2017.
- [41] Xiaolong Wang, Ross Girshick, Abhinav Gupta, and Kaiming He. Non-local neural networks. In *Proceedings of the IEEE conference on computer vision and pattern recognition*, pages 7794–7803, 2018.
- [42] Nan Chen, Wei Li, Charles Gatebe, Tomonori Tanikawa, Masahiro Hori, Rigen Shimada, Teruo Aoki, and Knut Stammes. New neural network cloud mask algorithm based on radiative transfer simulations. *Remote Sensing of Environment*, 219:62–71, 12 2018.
- [43] Stuart J Russell and Peter Norvig. *Artificial intelligence a modern approach*. London, 2010.
- [44] Gareth James, Daniela Witten, Trevor Hastie, Robert Tibshirani, et al. *An introduction to statistical learning*, volume 112. Springer, 2013.
- [45] NASA PACE Validation Plan, 2020. https://pace.oceansciences.org/docs/PACE_Validation_Plan_14July2020.pdf.
- [46] Steven A Ackerman, RE Holz, R Frey, EW Eloranta, BC Maddux, and M McGill. Cloud detection with modis. part ii: validation. *Journal of Atmospheric and Oceanic Technology*, 25(7):1073–1086, 2008.
- [47] Tao Wang, Eric J Fetzer, Sun Wong, Brian H Kahn, and Qing Yue. Validation of modis cloud mask and multilayer flag using cloudsat-calipso cloud profiles and a cross-reference of their cloud classifications. *Journal of Geophysical Research: Atmospheres*, 121(19):11–620, 2016.
- [48] A. Z. Kotarba. Calibration of global MODIS cloud amount using CALIOP cloud profiles. *Atmospheric Measurement Techniques*, 13(9):4995–5012, 2020.
- [49] RE Holz, SA Ackerman, FW Nagle, R Frey, S Dutcher, RE Kuehn, MA Vaughan, and B Baum. Global moderate resolution imaging spectroradiometer (modis) cloud detection and height evaluation using caliop. *Journal of Geophysical Research: Atmospheres*, 113(D8), 2008.
- [50] Steven Platnick, Kerry Meyer, Galina Wind, Robert E Holz, Nandana Amarasinghe, Paul A Hubanks, Benjamin Marchant, Steven Dutcher, and Paolo Veglio. The nasa modis-viirs continuity cloud optical properties products. *Remote sensing*, 13(1):2, 2020.
- [51] Max Kuhn, Kjell Johnson, et al. *Applied predictive modeling*, volume 26. Springer, 2013.
- [52] Leo Breiman. *Classification and regression trees*. Routledge, 1984.
- [53] Jerome Friedman, Trevor Hastie, and Rob Tibshirani. Regularization paths for generalized linear models via coordinate descent. *Journal of statistical software*, 33(1):1, 2010.